International Communications in Heat and Mass Transfer 165 (2025) 108999

Contents lists available at ScienceDirect

International Communications in Heat and Mass Transfer

journal homepage: www.elsevier.com/locate/ichmt

Investigating transient seepage flow and heat transfer using optical fiber distributed temperature sensors and hydrothermal modeling

Yaser Ghafoori [a,*], Stanislav Lenart [a], Uroš Bohinc [a], Andrej Kryžanowski [b]

[a] Slovenian National Building and Civil Engineering Institute, Dimičeva ulica 12, 1000 Ljubljana, Slovenia
[b] Faculty of Civil and Geodetic Engineering, University of Ljubljana, Jamova cesta 2, 1000 Ljubljana, Slovenia

ARTICLE INFO

Keywords:
Seepage
Phreatic line
Temperature
Heat dispersion
Optical fiber DTS

ABSTRACT

Seepage during the first filling of a reservoir is a critical aspect for earth dams and embankments safety, which requires precise monitoring. The thermometric method has demonstrated significant potential for detecting seepage anomalies through continuous temperature measurements using optical fiber distributed temperature sensing (DTS). However, most previous research has primarily focused on thermal monitoring when seepage flow reached a steady-state condition, which highlights the need for more research on seepage and heat transfer in transient state, particularly in unsaturated soils during the reservoir's first filling. This paper addresses the transient seepage flow and heat transfer during the first filling of a laboratory sand model. Temperature variations within the sand were recorded using an optical fiber DTS, while seepage progression was tracked through digital imaging at regular intervals, followed by image processing. A coupled hydrothermal numerical model was also developed to simulate transient seepage flow and heat transfer within the unsaturated and variably saturated sand. In numerical modeling, heat dispersion and the thermal conductivity of sand were investigated through parameter calibration. Results indicate that thermal monitoring using optical fiber DTS is an effective method for estimating the development of the phreatic line during the first filling of the reservoir. Numerical simulations further revealed that seepage velocity plays a key role in the heat transfer process during transient seepage. Additionally, the results highlight that heat dispersion significantly influences heat transfer, particularly during transient seepage flow, whereas the effect of thermal conductivity is relatively minor as seepage progresses.

1. Introduction

Seepage is the crucial factor in the health monitoring of earthen dams and embankments. Precise control and monitoring of seepage are essential, as excessive seepage can erode the soil particles and lead to internal erosion, the phenomenon behind 35 % of embankment failures [1]. The critical stage in the life of earth dams and embankments is the first filling of the reservoir. During this phase, the dam's body and foundation gradually saturate, resulting in consolidation and differential settlements. As the dam becomes saturated during the first filling, its weight increases, leading to a reduction in both shear strength and effective stresses. Most failures caused by internal erosion have been documented during or shortly after the first filling of the reservoir [2,3]. Notably, nearly 50 % of internal erosion failures in embankment dams occurred within the first year, emphasizing the critical need for efficient seepage monitoring at the early age of structures [4]. Although the duration and rate of the first filling vary for each dam, this process must always be carefully managed, controlled, and closely monitored to prevent adverse consequences.

The seepage field is characterized by examining the phreatic line, also referred to as the seepage line, within the earthen structure. The position of the phreatic line plays a crucial role in determining the stability of the dam [5]. Its development is typically assessed through analytical and numerical methods, along with physical model tests of the structure [6].

Application of temperature-based methods for seepage monitoring has gained significant attention, particularly with advancements in optical fiber distributed temperature sensing (DTS). In these methods, temperature variations measured by DTS using active (heat pulse) and passive approaches are analyzed to extract seepage-related information. The active method introduces a heat source into the dam body while DTS measures heat dissipation to detect seepage anomalies. The passive

* Corresponding author.
E-mail address: yaser.ghafoori@zag.si (Y. Ghafoori).

https://doi.org/10.1016/j.icheatmasstransfer.2025.108999

Available online 5 May 2025

method relies on natural soil temperature variations for seepage detection [7]. Several studies have explored both techniques to assess seepage characteristics, phreatic line development, and seepage-induced anomalies.

Su et al. 2018 [8] employed the heat pulse method with different heating power to analyze temperature fields above and below the phreatic line once steady-state seepage was established. Their findings indicated that temperature rise due to heating is smaller below the phreatic line, which provided a potential method for phreatic line estimation. Similarly, Cheng et al. 2021 [9] investigated phreatic line development under a constant hydraulic head using passive temperature measurements with over 10 m of optical fiber embedded in an experimental setup. Their study demonstrated the capability of passive temperature monitoring for estimating phreatic line development as seepage reaches steady-state conditions. Ma et al. (2023) [10] and Zhang et al. (2023) [11] demonstrated the effectiveness of passive temperature measurements in identifying structural damage and detecting leakage within the clay core of experimental earth-rock dam models. In their numerical modeling, Ma et al. (2023) [10] incorporated hydrothermal coupling in unsaturated soils, using the Van Genuchten equation to simulate the water retention curve. Li et al. (2024) [12] utilized heated optical fiber to investigate the seepage field in an experimental model. In combination with coupled seepage and temperature field modeling, they applied an inversion technique to estimate seepage velocity from the temperature measurements.

Furthermore, Nan et al. 2022 [13] conducted an experimental and numerical study to investigate the coupled hydrothermal process in soil, considering different methods for thermal conductivity estimation. Temperature sensor arrays were used to measure soil temperature under a constant hydraulic head. To enhance the spatial resolution of optical fiber measurements, Bekele et al. (2023) [14] proposed a method of wrapping the fiber around a PVC pipe for monitoring temperature fields in an experimental model under a constant water head [14,15]. While this approach significantly improved spatial resolution, the presence of PVC pipes influenced both seepage and temperature fields, as discussed in their findings.

Recent studies have also explored additional environmental influences on seepage-induced temperature variations. Zhang Tao and Su (2025) [16] examined the impact of seepage development on temperature fields using an optical fiber heat pulse method. Their study included the effects of reservoir water levels and rainfall, which revealed that water level variations had minimal influence on the temperature field within saturated zones.

Beyond small-scale laboratory models, optical fiber temperature measurement also has been applied in full-scale experimental levee models to assess seepage propagation [17] and evaluate its impact on levee failure due to overtopping [18].

Previous research works have focused on thermal monitoring as seepage flow reaches a steady-state condition [12,14] or on temperature monitoring of seepage through unsaturated soil under a constant water level [11,13]. While some experiments included transient seepage as it progressed toward steady-state, they did not examine temperature variations during this stage. As the first filling of the reservoir with a gradual water level rise is critical for seepage development and failure risks, further research is needed to investigate optical fiber DTS monitoring for phreatic line evaluation and transient seepage characterization in unsaturated soil during this stage.

In addition to experimental modeling, a coupled hydrothermal model can be effectively utilized to predict seepage behavior and thermal responses in embankment dams. Numerical simulations can be used to interpret DTS temperature data for the detection of singularities and unexpected seepage phenomena [19]. The conducted numerical modeling in the previous study mostly ignored the influence of heat dispersion [9,11,14] or used typical values from the literature review [10,20] in coupled hydrothermal analysis of seepage flow in soil. However, studies by Lu et al. (2018) [21] and Hopmans et al. (2002) [22] concluded that accounting for heat dispersion in coupled hydrothermal analysis significantly improves the estimation of water flux, particularly at higher flow velocities.

To address these gaps, this paper examines the phreatic line development in transient seepage flow through unsaturated sand during the first filling of a laboratory sand model. The phreatic line was assessed by numerical modeling, while temperature variations were recorded throughout the seepage experiment and the subsequent dewatering phase using an optical fiber DTS system. Over 130 m of optical fiber were embedded in the experimental model to provide a fully distributed thermal monitoring system.

Numerical modeling was conducted to simulate the transient seepage flow within the variably saturated sand. The numerical results were validated by comparing the computed saturation field with the results obtained from image processing. In addition, saturation at six reference points was verified using water level measurements from loggers embedded within the sand. Following validation, a coupled hydrothermal analysis was conducted which incorporated parameter calibration for heat dispersion and thermal conductivity of the sand grains to investigate their impact on the coupled seepage and heat transfer process.

2. Theory

The numerical calculation of seepage during the first filling of a reservoir is a complex transient problem, as the hydraulic properties of soil are highly dependent on its saturation state. The hydraulic head (piezometric head) is the sum of the pressure head (ψ) and the gravitational head (z, also called the elevation head); mathematically expressed as $h = \psi + z$. In variable saturation conditions, the pressure head is a function of the soil's saturation (s), denoted as $\psi(s)$. This relationship is described by the soil water characteristic curve (SWCC), or retention curve, which links the soil's saturation or water content to the negative pore pressure (suction).

The hydraulic conductivity of soil is a function of its degree of saturation too, as defined by the relative conductivity curve. This curve represents the hydraulic conductivity of soil under varying saturation conditions. The hydraulic conductivity tensor $\boldsymbol{k}(s)$ is the product of saturated hydraulic conductivity ($\boldsymbol{k}$) and the relative conductivity parameter $k_r(s)$ [23].

$$\boldsymbol{k}(s) = k_r(s).\boldsymbol{k} \tag{1}$$

The Richards equation, derived from the principles of mass continuity and Darcy's law, is commonly used to evaluate seepage flow in unsaturated soil. In Eq. (2), n represents porosity, and t denotes time.

$$n\frac{\partial s}{\partial t} - \nabla \bullet [k_r(s).\boldsymbol{k}.\nabla(\psi + z)] = 0 \tag{2}$$

For practical applications, heat transfer in soil is primarily governed by conduction and convection due to seepage flow, while the influence of radiation is typically neglected. In most natural porous media, local thermal equilibrium between the fluid and solid phases is assumed, meaning the temperatures of the fluid and solid grains are equal. In unsaturated soils, heat conduction in the pores is a two-phase process, where both water and air trapped within the pores contribute to heat transfer. Heat transfer within the soil is described by the energy balance equation under the assumption of local thermal equilibrium [24].

$$\rho c\frac{\partial T}{\partial t} + \rho_f c_f.\mathbf{v}.\nabla T = \nabla \bullet (\lambda \nabla T) + q'' \tag{3}$$

where ρ, c and λ are the soil density, specific heat capacity, and thermal conductivity, respectively, while T denotes the temperature of soil. $\mathbf{v}$ is the flow Darcy velocity vector, ρ_f and c_f refer to the fluid density and specific heat capacity and q'' is the volumetric heat generation in soil. The effects of heat dispersion must also be considered. Eq. (3) is

Table 1
Material properties of the sand.

k_{sat} (m/s)	G_s (g/cm^3)	ρ_d (g/cm^3)	n
1.23×10^{-3}	2.7	1.54	0.435

modified by neglecting heat generation and incorporating the heat dispersion tensor ($\boldsymbol{D}$) [25].

$$\rho c \frac{\partial T}{\partial t} + \rho_f c_f . \mathbf{v} . \nabla T = \nabla \bullet (\lambda \nabla T) + n \rho_f c_f (\boldsymbol{D} . \nabla T) \tag{4}$$

Heat dispersion in porous media depends on several factors, including flow velocity, the structure of the medium, porosity, the ratio of thermal conductivities, and the ratio of volumetric heat capacities between the solid and fluid phases [26]. In an isotropic medium, the heat dispersion tensor in local coordinates forms a diagonal matrix with non-zero components, which can be expressed in terms of longitudinal and transverse dispersion coefficients [25,27].

$$D_{ij} = \beta_t |\mathbf{v}| \delta_{ij} + (\beta_l - \beta_t) \frac{\mathbf{v} \otimes \mathbf{v}}{|\mathbf{v}|} \tag{5}$$

here, β_l and β_t represent the longitudinal and transverse dispersivity coefficients of soil, respectively, and δ_{ij} is the Kronecker delta.

In unsaturated soils, thermal properties are influenced by the degree of saturation. Under the assumption of local thermal equilibrium, the thermal conductivity (λ) and volumetric heat capacity (ρc) of the soil can be calculated as the weighted arithmetic means of the solid and fluid phases [28].

$$\rho c = (1-n)\rho_s c_s + ns\rho_w c_w + n(1-s)\rho_g c_g \tag{6}$$

$$\lambda = (1-n)\lambda_s + ns\lambda_w + \mathrm{n}(1-s)\lambda_g \tag{7}$$

where subscripts s, w, and g represent the solid grain, water, and air, respectively.

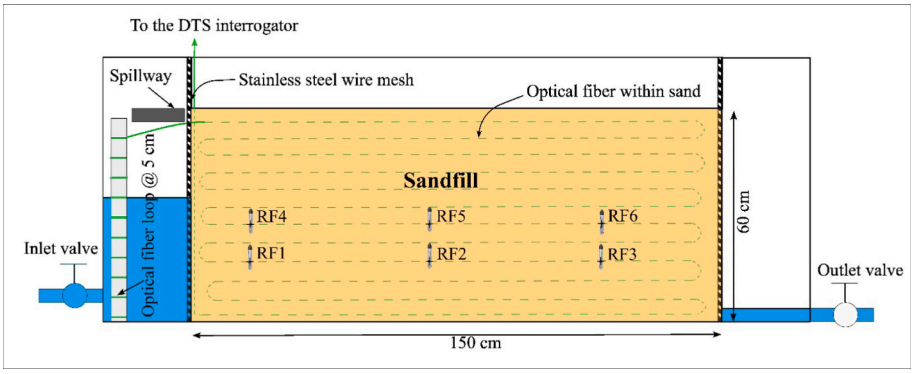

(a)

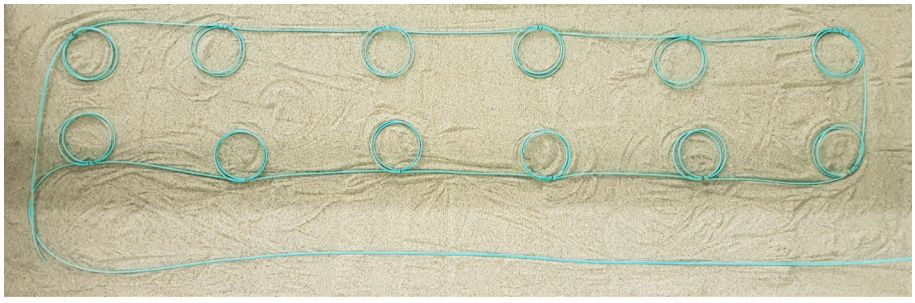

(b)

(c)

Fig. 1. (a) Details of experimental model; (b) Top view of optical fiber placement; (c) Side view of sand-fill box.

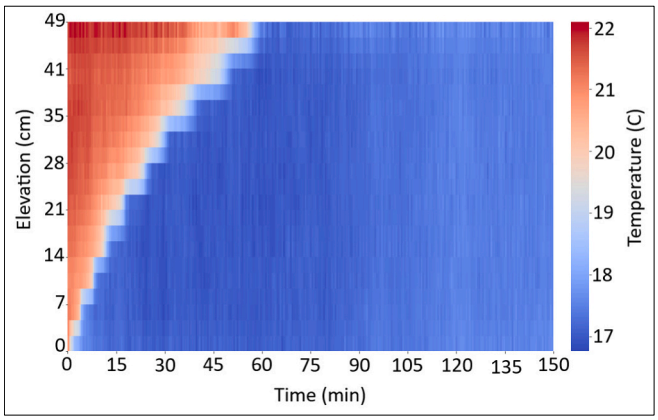

(a)

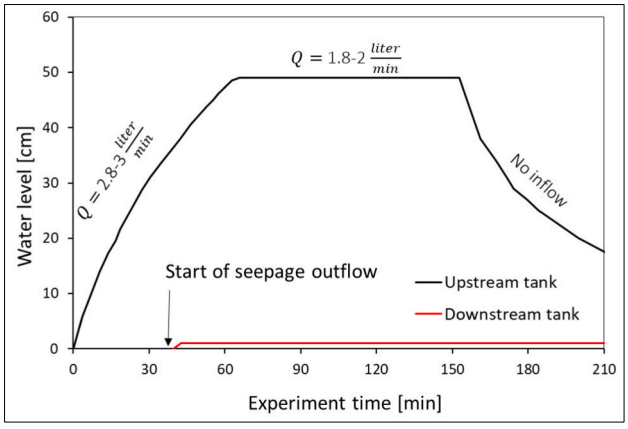

(b)

Fig. 2. (a) Temperature at the upstream boundary due to water raising; (b) Water level at upstream and downstream.

Table 2
Hydraulic and thermal properties of sand.

Van Genchten parameters for SWCC and k_r cure				Volumetric heat capacity of grains	Volumetric heat capacity of water	Thermal conductivity of water
g_a	g_n	g_m	g_l	$(\rho c)_s$	$(\rho c)_f$	λ_f
9.67	8.06	0.876	2.2	$2\ \frac{MJ}{m^3k}$ [34]	$4.2\ \frac{MJ}{m^3k}$	$0.65\ \frac{W}{mk}$

Table 3
Numerical models to calibrate heat dispersion and thermal conductivity of grain particles.

Model	λs [W/mK]	βl [m]	βt [m]	Model	λs [W/mK]	βl [m]	βt [m]
M1	2.7	0.005	0.003	M10	4.0	0.050	0.030
M2	2.7	0.050	0.030	M11	4.0	0.100	0.050
M3	2.7	0.500	0.300	M12	4.0	0.500	0.300
M4	2.7	1.000	0.500	M13	4.0	1.000	0.500
M5	3.2	0.005	0.003	M14	4.0	1.000	1.000
M6	3.6	0.005	0.003	M15	4.3	0.005	0.003
M7	4.0	0.000	0.000	M16	4.3	0.050	0.030
M8	4.0	0.005	0.003	M17	4.3	0.500	0.300
M9	4.0	0.010	0.005	M18	4.3	1.000	0.500

3. Methodology

3.1. Material

Silica-dominated sand, sourced from a local vendor, was used in the laboratory experiment. The saturated hydraulic conductivity of the sand (k_{sat}) was measured according to ASTM D2434 using a constant head rigid wall permeameter. The porosity of the material was calculated based on laboratory measurements of the dry density and particle density of the silica sand. The material properties of the sand used in the experiment are presented in Table 1.

The soil water characteristic curve (SWCC) and relative hydraulic conductivity of the sand were determined using the evaporation method with the HYPROP device [29]. In numerical modeling, the modified van Genuchten equation [30] was applied to describe the sand's behavior in unsaturated conditions, with its parameters fitted to the HYPROP data for both SWCC and the relative hydraulic conductivity curve. Detailed results of the SWCC and relative hydraulic conductivity are presented in [19].

A passive optical fiber interrogator (SILIXA XT-DTS) [31] was employed with a 50/125 multi-mode optical fiber cable. Two PT-100 thermometers were integrated into the system and served as the system references. Temperature measurements were conducted using the duplexed single-ended installation approach [32], which allows two temperature readings per point. To improve temperature measurement resolution, optical fiber coils (sensory rings) with a perimeter of 50.8 cm were formed, as shown in Fig. 1(b).

The spatial resolution and time response of the optical fiber DTS were determined through laboratory experiments to be 0.63 m and 60 s, respectively [19]. The efficiency of the fiber coil setup was tested through a laboratory experiment where four successive fiber coils of varying lengths (25.4 cm, 50.8 cm, 101.6 cm, and 203.2 cm) were immersed in an insulated tub of hot water. This experiment demonstrated the impact of spatial resolution on detecting abrupt temperature changes.

Additionally, temperature and hydraulic head were measured at six reference points (RFs) within the sand using water level loggers. These loggers provided temperature measurements with a maximum error of 0.4 °C and water level measurements with a maximum error of 0.6 cm [33].

3.2. Experimental setup

An experimental model consisting of a box with dimensions of 150 cm × 50 cm × 60 cm was designed and constructed. The box was filled with 700 kg of sand, which was compacted to match the bulk density used in the laboratory tests for saturated hydraulic conductivity. Seepage was induced from an upstream tank, separated from the sand by a steel wire mesh with openings large enough to allow free seepage flow.

A total of 130 m of optical fiber was embedded in the sand across 12 vertical layers. The precise location of the cable within the sand was recorded relative to the DTS system, which was essential for accurately mapping the reported temperature along the cable $T(x,t)$ to the spatial coordinates $T(X,Y,Z,t)$ within the sand model. The DTS system was set to a sampling interval of 10 in. (25.4 cm) with an acquisition time of 30 s. The optical fiber DTS provided 520 temperature measurements throughout the entire sand model. Six reference points (see Fig. 1(a)) were established at two different elevations, equipped with temperature and water level loggers.

Digital images were captured at regular intervals through a side Plexiglas plate to monitor seepage propagation. The heat boundary effect was minimized using the Plexiglas at the side and an insulation layer installed at the bottom of the model. The water level rise in the upstream tank, along with the inflow rate, was measured regularly. The outlet valve at the downstream tank was opened to allow the seepage to flow freely out of the model. Temperature at the upstream tank was

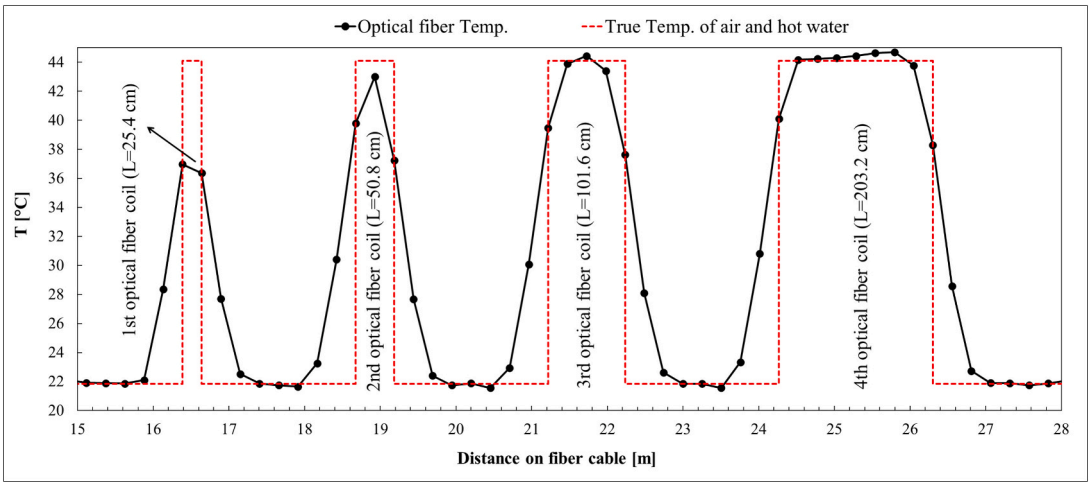

Fig. 3. Temperature measurement by fiber coils with different perimeters.

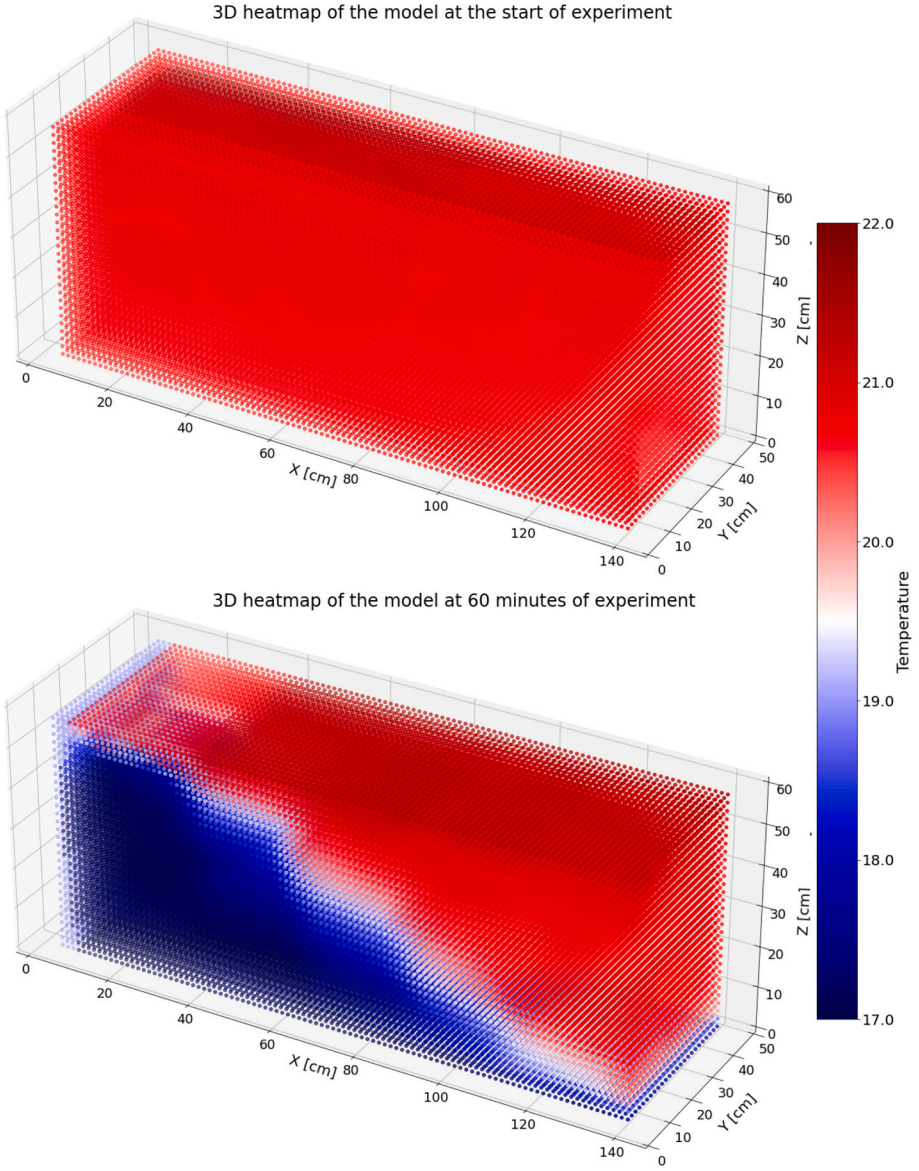

Fig. 4. 3D heatmap of sandfill model at the start of the experiment and at 60 min.

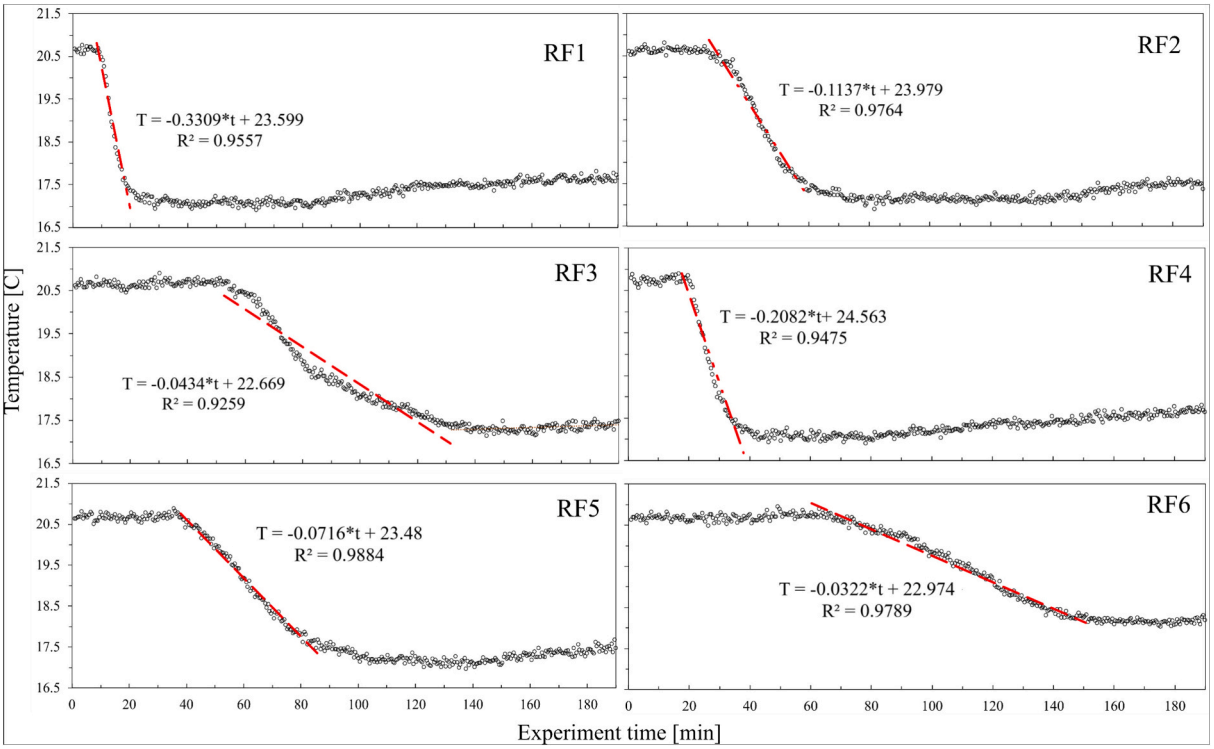

Fig. 5. Temperature measured by optical fiber in reference points during the experiment.

continuously measured during the water level rise at 10 elevations, using optical fiber coils with a 1-m length. Water with a constant temperature of 17 ± 0.1 °C was used in the experiment. Over time, the water temperature in the upstream tank was slightly increased due to the influence of higher ambient temperatures in the laboratory. The measured temperature in the upstream tank during the experiment was in a range from 17.0 to 17.5 °C.

The experiment began with an inflow rate of 2.8–3 L/min and continued until the water level reached the maximum spillway elevation (49 ± 0.2 cm). The inflow rate was then reduced to 1.8–2 L/min to maintain a constant water level in the upstream tank until two and a half hours, after which the inflow gauge was closed. At steady-state flow, the water level in the downstream tank stabilized at 1 cm. The heatmap of temperature measured at the upstream tank is shown in Fig. 2(a), while the water levels at both the upstream and downstream tanks are displayed in Fig. 2(b).

Statistical analysis was performed using the NumPy and Matplotlib Python libraries to interpolate temperature measurements and determine the temperature distribution during the seepage experiment. The ordinary Kriging method, with a linear variogram model, was applied for temperature data interpolation. Image processing was also carried out on the captured images during the experiment to monitor the development of the saturation field. Image thresholding was used to enhance the contrast between the dry and wet zones, followed by the application of the Convex hull algorithm to identify and extract the boundary between the wet and dry sand.

3.3. Numerical modeling

Two-dimensional (2D) numerical modeling was performed using FEFLOW (version 7.2) software, based on the vertical planar projection of the sand fill. The model assumed a homogeneous, isotropic sand fill, with the effects of the optical fiber on seepage flow and thermal properties considered negligible. The model was discretized into 28,588 three-node triangular elements, with finer mesh applied near the upstream boundary.

Based on experimental measurements, the sand was initially considered dry at its residual water content, with a constant temperature of 20.9 °C. A time-dependent hydraulic head was applied to the upstream face, based on water level measurements from the experiment (see Fig. 2(b)). The downstream and top boundaries were defined as seepage faces (free seepage) which allow fluid outflow at atmospheric pressure when fully saturated. The bottom boundary was set as a closed boundary. The thermal boundaries were defined based on the experimental conditions. A time-dependent temperature was applied to the upstream boundary nodes, using the temperature measurements obtained from the optical fiber coils (see Fig. 2(a)). The top and downstream boundaries were set to a constant ambient temperature, while the bottom boundary was insulated with thin layers of epoxy.

Initially, transient seepage flow within the unsaturated and variably saturated sand was simulated. The numerical model was validated by comparing its results with those obtained from image processing and water level measurements at the reference points. A coupled hydrothermal analysis was then conducted to evaluate the heat transfer process during the seepage experiment.

The thermal and hydraulic properties of the sand were obtained either from the laboratory measurements or calibrated from the suggested values in literature. The dependency of material properties on the degree of saturation was incorporated into the numerical modeling, as outlined in Section 2. The water retention and relative hydraulic conductivity curves were assigned by fitting the parameters of the modified Van Genuchten equation to the measured HYPROP data. Detailed descriptions of these parameters can be found in [19,25]. Table 2 presents the thermal and hydraulic properties of the sand as used in the numerical modeling.

The thermal conductivity of sand was calculated using Eq. (7) for various degrees of saturation. However, the thermal conductivity of silica quartz grain particles has been reported with a wide range of variation in different studies [22,35,36]. In addition, heat dispersion coefficients must also be considered in the coupled hydrothermal analysis. A parameter calibration study was conducted, testing different values for grain thermal conductivity and heat dispersion coefficients to

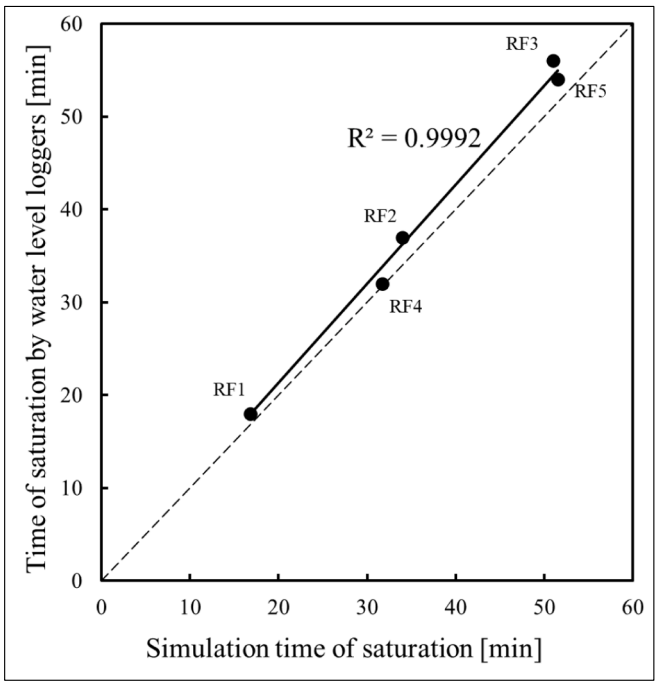

(a)

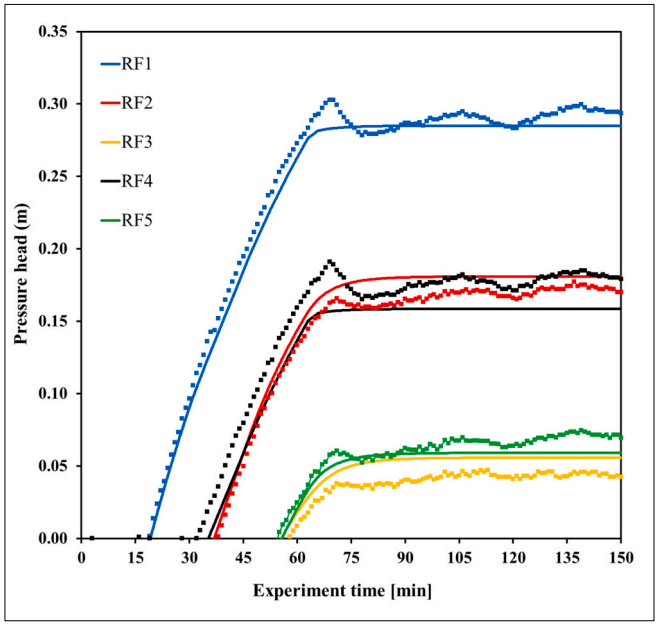

(b)

Fig. 6. Comparison of numerical results with reference loggers' measurements; (a) saturation time; (b) pressure head (dashed lines are the loggers' measurements).

evaluate their impact on the thermal behavior of unsaturated soil under seepage flow. Table 3 presents the numerical models and associated parameter values used in the calibration study.

4. Results and discussion

Temperature measurements within the sand were conducted using fiber optic DTS during the seepage experiment and at six reference points with loggers for long-term monitoring, both before and after the experiment. The application of optical fiber coil was examined in terms of resolution enhancement. Fig. 3 shows temperature measurements from four fiber coils of varying perimeters. The figure highlights two key findings: First, an abrupt temperature change may be missed by the DTS when the cable segment exposed to the change is shorter than the system's spatial resolution, as observed with the 25.4 cm coil. Secondly, sampling intervals located at the center of the fiber coil provide the most accurate temperature readings, as boundary intervals are influenced by adjacent fibers. The fiber coil with a 50.8 cm perimeter, used in this study, provided temperature measurements with 95 % expected precision. In the application of fiber coil, care should be taken that the bending of the cable be bigger than the minimum bending allowed by the manufacturer of the fiber and interrogator system to avoid breakage of the fiber or significant loss of light power.

The optical fiber embedded within the sand reported 520 temperature points at 30-s intervals, which provides fully distributed, continuous measurements throughout the seepage experiment. A 3D heatmap of the sand box, generated from the DTS measurements, is shown in Fig. 4, which depicts the start of the experiment and at 60 min through the experiment. The figure clearly demonstrates that the temperature distribution within the sand is influenced by the propagation of seepage, with the sand temperature decreasing as the seepage progresses.

The temperature variations for six reference points (RFs, see Fig. 1) are illustrated in Fig. 5. As shown, the temperature change during the experiment at each point follows three distinct phases: a) the dry stage occurs before water reaches the point, during which the soil remains unsaturated and the temperature stays stable; b) the transition stage as the soil gradually saturates and the temperature decreases; and c) the third stage as the temperature approximately stabilizes before the dewatering phase of the model. At the end of the third stage, the soil temperature increases by approximately 0.5 °C due to the rise in upstream water temperature from 17.0 °C to 17.5 °C.

To estimate the rate of temperature change, a linear regression analysis was performed for each RF during the transition stage. The regression results indicate a relatively strong linear relationship, which show the consistency of rate of temperature change during this stage. The slope of the regression line represents an estimate of the thermal velocity at each point. It was observed that the rate of temperature drop varies across different reference points. While RF1 and RF4 at the upstream boundary experience a steep temperature drop, the temperature change at RF3 and RF6, near the downstream boundary, occurs much more gradually.

The numerical simulation of transient seepage flow was conducted for 150 min to evaluate the development of saturation and Darcy flux in unsaturated and variably saturated sand. Water level loggers continuously recorded pressure head and temperature variations at six RFs within the sand, as shown in Fig. 1(a). It should be noted that the logger at RF6 was unable to report pressure head measurements due to a malfunction. The simulation was validated by comparing the computed saturation and pressure head results with the measurements from the five functional reference points. Fig. 6(a) compares the time at which the five reference points reached full saturation in the simulation with saturation time measured by the water level loggers. Fig. 6(b) shows the pressure head development at the reference points, comparing numerical results (continuous line) with logger measurements (dashed line).

As shown in Fig. 6, the numerical simulation aligns well with the experimental measurements in terms of saturation degree and pressure head, which confirms the assumptions made during numerical modeling, particularly regarding the assignment of water retention and relative hydraulic conductivity curves using the modified Van Genuchten equation.

Image processing was performed on photos captured at one-minute intervals during the experiment to extract the boundary between the wet and dry sand, here, referred to as the apparent moisture boundary (AMB). In Fig. 7(a), the AMB is highlighted in red and compared with the phreatic line from the numerical simulation (line 1) and the line representing 90 % saturation (line 0.9). Each image corresponds to the experiment time when the temperature starts to decrease at a reference

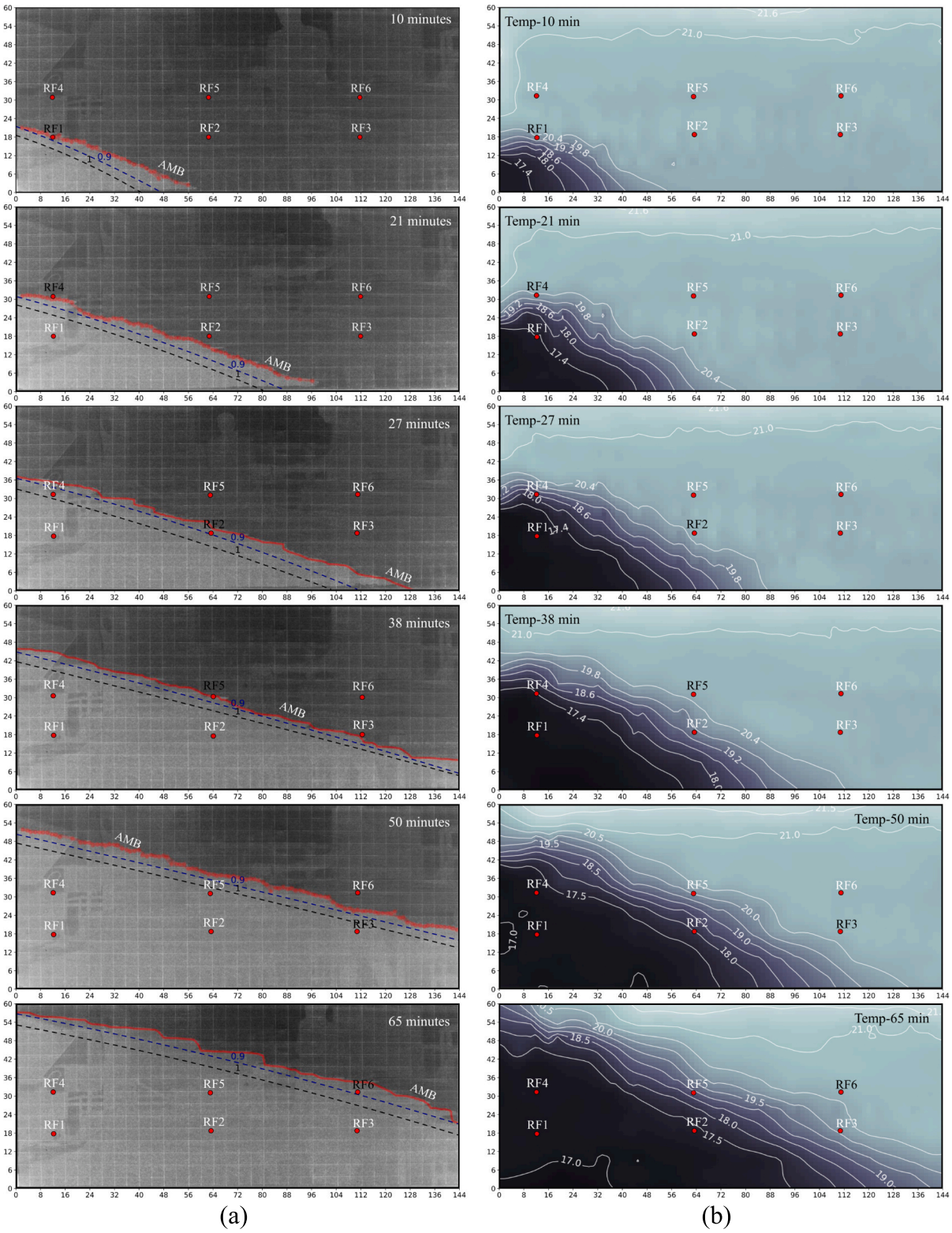

Fig. 7. (a) Comparison of numerically computed saturation with the AMB obtained from processed images; (b) Heatmap of temperature distribution within the sand.

point. The associated RF is marked in black in each image for distinction. The results indicate that the interface between the dry soil and partially moist soil was effectively estimated through image processing of captured digital images using image thresholding techniques in Python. To compare the saturation development with the temperature variation, the temperature distribution in a vertical planar projection of the sand model is visualized using Kriging interpolation in Fig. 7(b). As shown, the temperature decline in each RF begins as soon as the saturation line reaches that point.

Additionally, Fig. 8 displays the numerically calculated saturation line (NSL) overlaid on the heatmap of the sand model. A clear correlation is observed between the development of the phreatic line and the temperature distribution within the sand, which indicates the relationship between saturation and the heat transfer process.

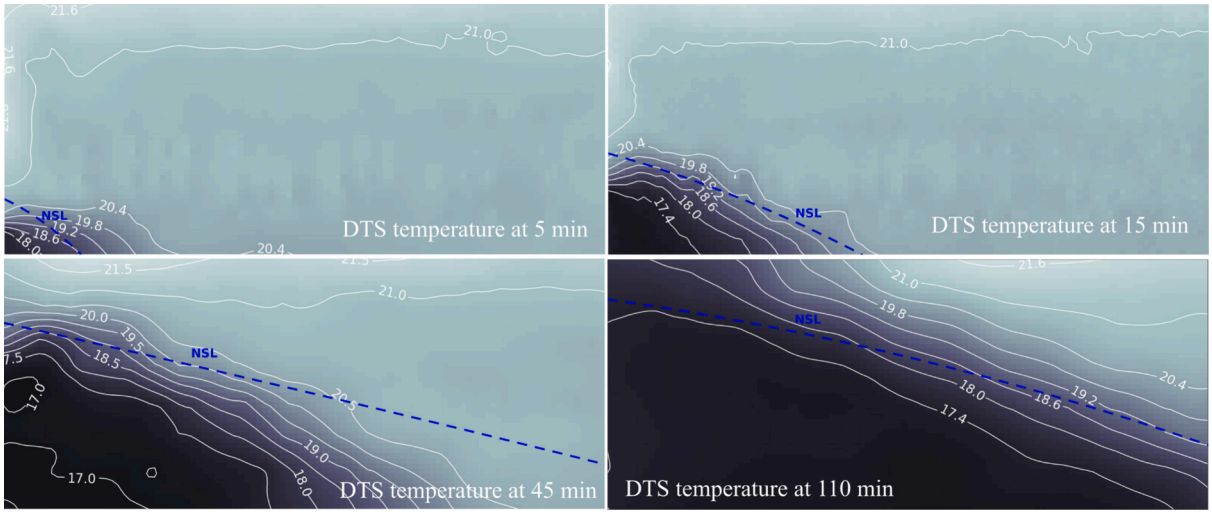

Fig. 8. Numerically calculated seepage line (NSL) on the heatmap of sand model.

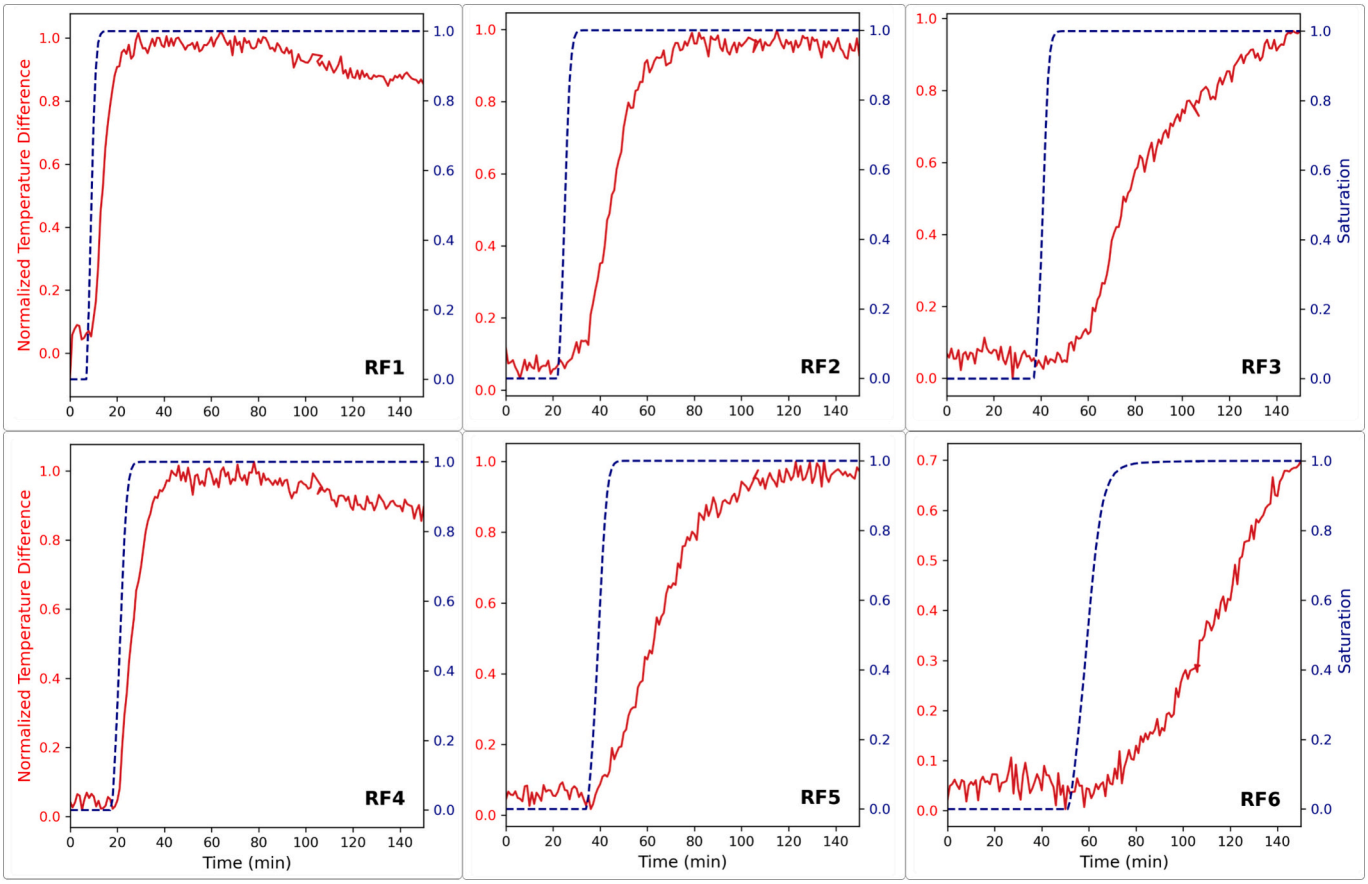

Fig. 9. Comparison of normalized temperature difference from optical fiber measurements and degree saturation from numerical modeling.

The normalized temperature differences for RFs are calculated and presented together with the saturation degree curve in Fig. 9. It is observed that temperature changes occur as soon as the saturation degree begins to increase. However, a short time gap is particularly noticeable for RF3 and RF6 between the increase in saturation degree and the temperature decline. This indicates that the temperature change during this short period was less than the detection resolution of the optical fiber DTS system, and therefore, it was not recorded by the sensor. As also observed in Fig. 5, the rate of temperature change varies across different locations. At the upstream boundary, where cold water first enters, the temperature drops sharply as the water immediately cools the surrounding soil. However, as seepage progresses deeper into the model, the specific heat capacity of the soil causes a delay in temperature reduction and time is required for the soil to fully adjust to the new thermal conditions. At each point, the infiltrating water reaches thermal equilibrium with the sand particles and stabilizes at a new temperature. This water, now at a modified temperature, then moves deeper into the dry sand. As seepage continues, flowing water gradually

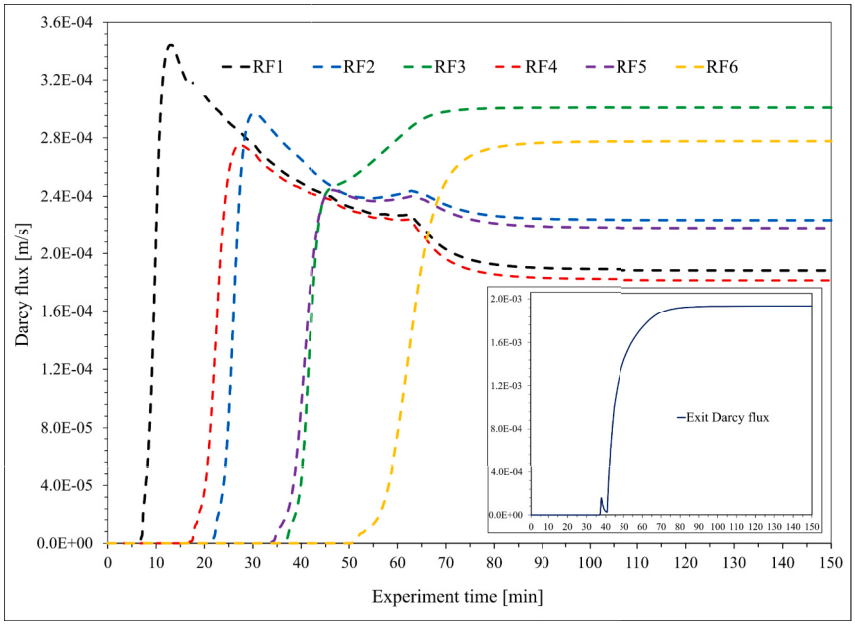

(a)

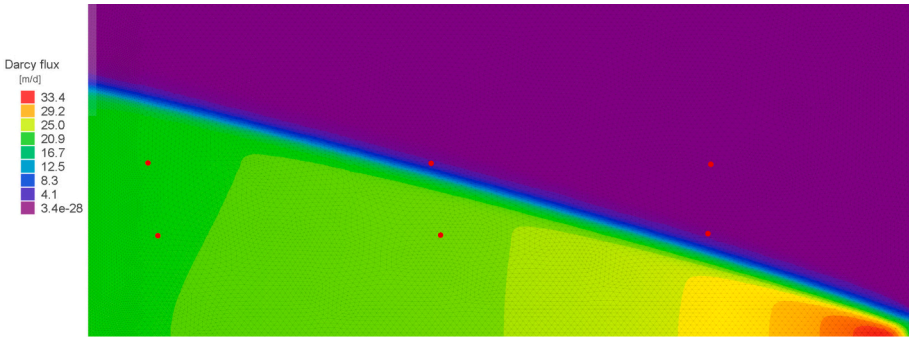

(b)

Fig. 10. Numerical results of Darcy velocity; a) RFs and exit point; and b) Darcy velocity at 38 min of experiment.

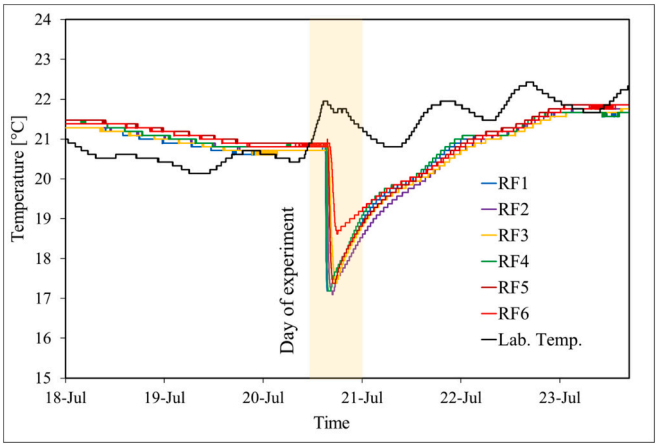

Fig. 11. Temperature in reference points measured by temperature loggers.

transfers heat and eventually imposes the upstream boundary temperature onto the soil. As a result, the farther a point is from the upstream cold-water front, the slower its temperature decreases.

The Darcy velocity is illustrated in Fig. 10(a) for the six RFs and the exit point where the seepage flowed out of the model at the downstream boundary. The rate of temperature decline (thermal velocity) is also strongly influenced by the magnitude of the Darcy velocity: the higher the Darcy velocity, the faster the temperature drop. At 38 min into the experiment, water exits the model with a significantly higher Darcy velocity compared to other locations, as shown in Fig. 10(b).

After the seepage inflow was stopped and dewatering began within the sand, the temperature within the sand slowly increased due to thermal conduction. This is a gradual process, as conduction is slower compared to convection, and it takes longer for the soil to reach thermal equilibrium with the ambient temperature. Fig. 11 shows the temperature measurements at six RFs before, during, and after the experiment. As seen in this figure, it takes more than 2 days for the soil to reach thermal equilibrium with the laboratory temperature after the dewatering process begins.

The saturation front advances ahead of the heat flow due to the difference between seepage velocity and thermal velocity. Thermal velocity is influenced by the soil's thermal conductivity and heat capacity in dry sand, but once seepage occurs, convective heat transfer becomes the dominant mechanism, with seepage velocity playing a key role in the heat transfer process. As seen in Fig. 11, heat transfer by convection with seepage flow is much faster than thermal conduction.

The optical fiber DTS detects small temperature variations within the sand, driven by convective heat transfer as water propagates through and fills the pores between the particles. The development of the phreatic line within unsaturated soil significantly affects the soil's thermal

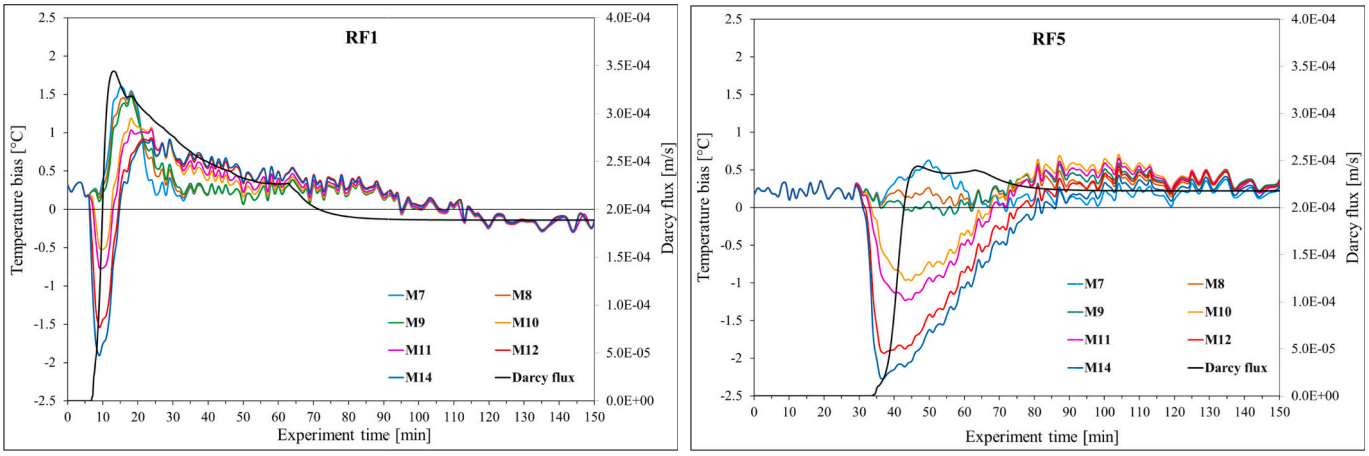

Fig. 12. Thermal analysis of sand with different thermal dispersion coefficients for RF1 and RF5 points; (a) DTS temperature variation and computed Darcy velocity; (b) computed temperature bias to DTS measurements.

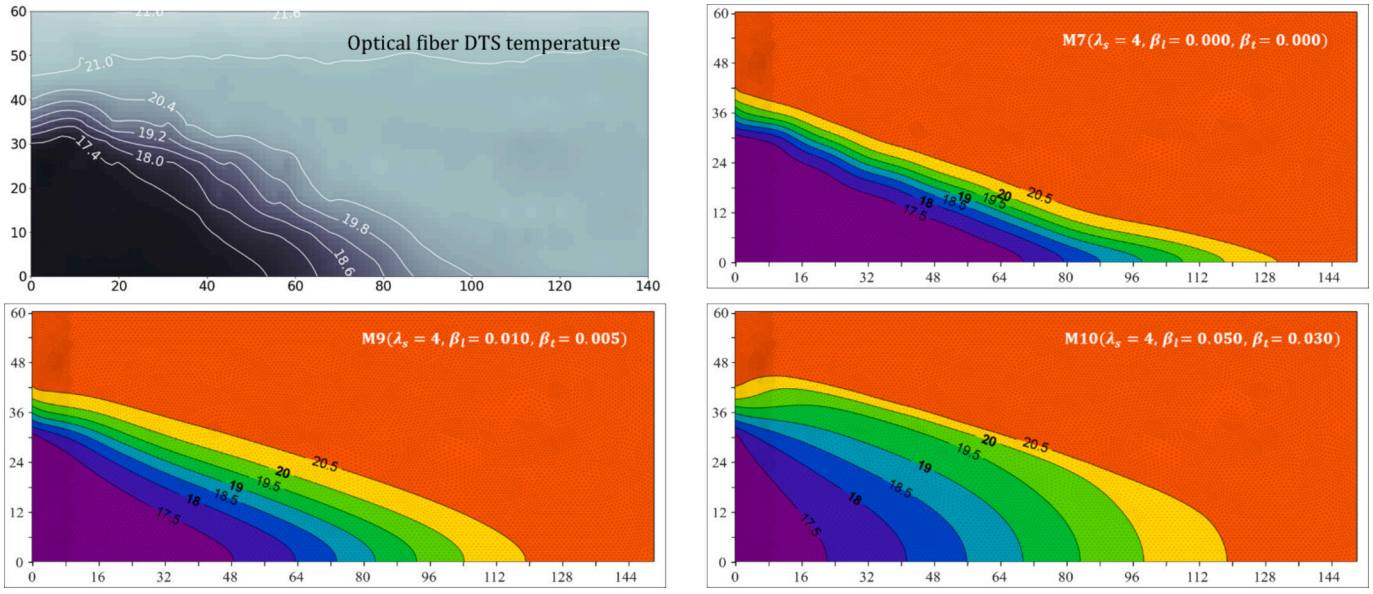

Fig. 13. Heat distribution within sand at 35 min measured by optical fiber DTS and numerical results.

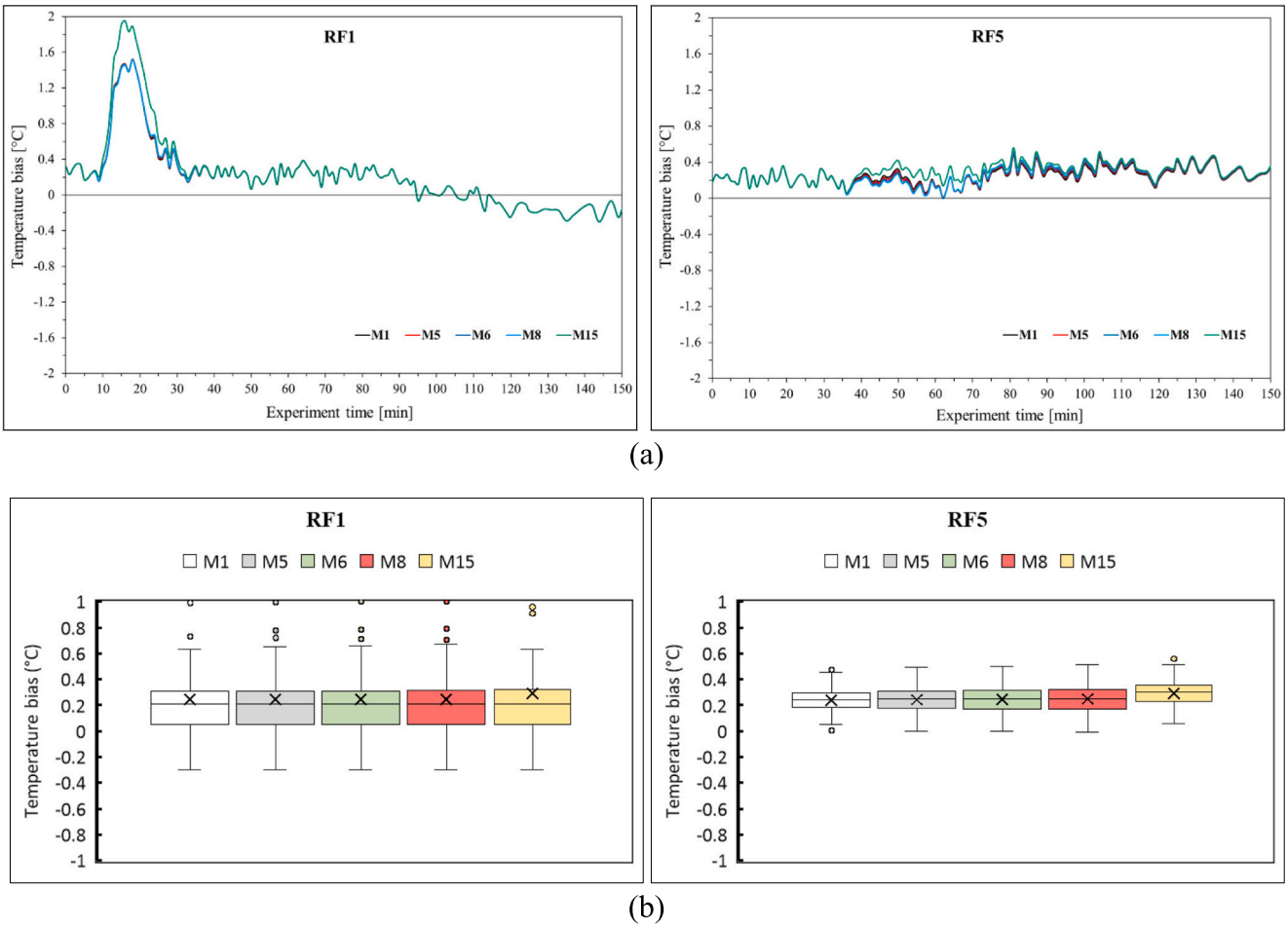

Fig. 14. Thermal analysis of sand with different solid thermal conductivities for RF1 and RF5 points. (a) DTS temperature variation and computed Darcy velocity; (b) computed temperature bias to DTS measurements.

state, making thermal monitoring an effective method for estimating the phreatic line's location. A temperature decline occurs as soon as the saturation front reaches the measurement points.

Seepage flow plays a crucial role not only in heat transfer by convection but also as a key factor in heat dispersion. The influence of heat dispersion and conduction in coupled hydrothermal analysis was investigated through numerical modeling and parameter calibration. The validated seepage model was enhanced for hydrothermal analysis by considering different values for heat dispersion coefficients and thermal conductivities. Fig. 12 presents the thermal analysis results, showing the temperature differences between the numerical simulations and DTS measurements at two reference points. The analysis incorporates models with constant thermal conductivity and variable longitudinal and transverse heat dispersivity coefficients (as detailed in Table 3).

As expected from the energy balance equation, heat dispersion does not influence the thermal behavior of soil in the absence of seepage flow. However, once seepage begins and the Darcy velocity deviates from zero, heat dispersion effect becomes evident. It can be seen that heat dispersion is significant in coupled hydrothermal analysis when the Darcy velocity increases, causing heat dispersion occurs faster due to seepage flow. The influence of dispersion is most notable during transient seepage conditions, but as seepage reaches the steady-state condition and the velocity stabilizes, the significance of dispersion decreases. This is observed in Fig. 12(a), where steady-state conditions are established approximately 63 min after the start of the seepage experiment. The impact of heat dispersion is also demonstrated in Fig. 13, where the temperature distribution obtained from optical fiber DTS is compared with three thermal analysis models using different heat dispersivity coefficients at 35 min into the experiment.

The influence of thermal conduction during the transient seepage flow was studied by conducting numerical modeling considering different thermal conductivity values. As shown in Eq. (7), while the thermal conductivity of water and air remains relatively constant, the thermal conductivity of solid grains is the only variable, with significant variation reported in the literature. The computed temperatures at two reference points for different numerical models are presented in Fig. 14, where all other thermal properties remain constant, and only the thermal conductivity of the solid grains is varied (see Table 3).

As shown, the influence of thermal conductivity is minimal during the heat transfer process when seepage flow is in progress. This indicates that heat conduction becomes less effective, and heat transfer occurs almost entirely through convection driven by the seepage flow. Even during dewatering, when water flows out of the model, it takes a significantly longer time for the temperature to return to its initial state and reach equilibrium with the ambient temperature. This is due to the low thermal velocity associated with heat conduction.

5. Conclusion

An experimental and numerical study was conducted to evaluate transient seepage flow within variably saturated sand during the first filling of a sand model. The temperature of the sand was measured using 130 m of optical fiber, forming a fully distributed continuous sensor within the model. The numerical modeling of seepage flow was validated by experimental measurements. A coupled hydrothermal analysis

was performed, focusing on the effect of heat dispersion and heat conduction during the transient seepage. The findings of this study lead to the following conclusions:

- Thermal monitoring using passive optical fiber DTS is an effective method for estimating the progress of the phreatic line during the first filling of the reservoir.
- The phreatic line precedes the thermal front within the sand. The temperature change in dry sand occurs as soon as the saturation degree increases. However, the rate of temperature change depends on the Darcy velocity of seepage and the distance of the point from the reservoir.
- The thermal velocity due to heat convection by seepage flow is a far faster process than heat conduction.
- Seepage flow is the primary factor driving heat transfer during transient seepage in variably saturated soil. It controls heat convection, the dominant heat transfer mechanism, and significantly influences heat dispersion.
- Coupled hydrothermal analysis shows that heat dispersion plays a significant role during transient seepage flow, with its influence increasing as Darcy velocity changes and diminishing as seepage flow stabilizes.
- Heat conduction has a minor effect on the heat transfer process when seepage flow is active within the soil.

CRediT authorship contribution statement

Yaser Ghafoori: Writing – review & editing, Writing – original draft, Visualization, Validation, Software, Methodology, Investigation, Formal analysis, Data curation, Conceptualization. **Stanislav Lenart:** Writing – review & editing, Writing – original draft, Supervision, Resources, Funding acquisition. **Uroš Bohinc:** Writing – review & editing, Visualization, Validation, Methodology. **Andrej Kryžanowski:** Writing – review & editing, Supervision, Resources, Funding acquisition.

Declaration of competing interest

The authors declare that they have no known competing financial interests or personal relationships that could have appeared to influence the work reported in this paper.

Yaser Ghafoori reports financial support was provided by Slovenian Research and Innovation Agency. If there are other authors, they declare that they have no known competing financial interests or personal relationships that could have appeared to influence the work reported in this paper.

Acknowledgments

The author's contribution is originally based on his research work at the University of Ljubljana, Faculty of Civil and Geodetic Engineering, which was financially supported by the core funding (No. P2-0180) covered by the Slovenian Research and Innovation Agency (ARIS). The authors also acknowledge the support from the Slovenian Research and Innovation Agency (research core funding No. P2-0273, Building Structures and Materials) and the Interreg Danube Region project DRP0200484 – SAFETY4TMF.

Data availability

The data that support the findings of this study are available from the corresponding author upon request.

References

[1] Q. Zhong, et al., Breaches of embankment and landslide dams - state of the art review, Earth Sci. Rev. 216 (2021) 103597, https://doi.org/10.1016/j.earscirev.2021.103597.
[2] L. Zhang, M. Peng, D. Chang, Y. Xu, Dam failure mechanisms and risk assessment, in: Dam Failure Mechanisms and Risk Assessment, 2016, pp. i–xix, https://doi.org/10.1002/9781118558522.fmatter.
[3] N.M. Rana, et al., Global magnitude-frequency statistics of the failures and impacts of large water-retention dams and mine tailings impoundments, Earth Sci. Rev. 232 (2022) 104144, https://doi.org/10.1016/j.earscirev.2022.104144.
[4] ICOLD Committee on Dam Safety, ICOLD Incident Database Bulletin 99 Update: Statistical Analysis of Dam Failures, Int. Comm. Large Dams, Paris, 2019.
[5] L. Dong, D. Sun, X. Li, Theoretical and case studies of interval nonprobabilistic reliability for tailing dam stability, Geofluids 2017 (2017) 8745894, https://doi.org/10.1155/2017/8745894.
[6] Z. Lyu, J. Chai, Z. Xu, Y. Qin, J. Cao, A comprehensive review on reasons for tailings dam failures based on case history, Adv. Civil Eng. 2019 (2019) 4159306, https://doi.org/10.1155/2019/4159306.
[7] Y. Ghafoori, A. Vidmar, J. Říha, A. Kryžanowski, A review of measurement calibration and interpretation for seepage monitoring by optical fiber distributed temperature sensors, Sensors 20 (19) (2020) 1–23, https://doi.org/10.3390/s20195696.
[8] H. Su, H. Li, Y. Kang, Z. Wen, Experimental study on distributed optical fiber-based approach monitoring saturation line in levee engineering, Opt. Laser Technol. 99 (2018) 19–29, https://doi.org/10.1016/j.optlastec.2017.06.032.
[9] L. Cheng, A. Zhang, B. Cao, J. Yang, L. Hu, Y. Li, An experimental study on monitoring the phreatic line of an embankment dam based on temperature detection by OFDR, Opt. Fiber Technol. 63 (2021) 102510, https://doi.org/10.1016/j.yofte.2021.102510.
[10] Z. Ma, J. Ren, L. Zhang, H. Li, S. Yang, S. Nan, Monitoring heat transfer for seepage in earth-rock dams with clay cores considering damaged areas: laboratory experiments and numerical modeling, Comput. Geotech. 164 (2023) 105833, https://doi.org/10.1016/j.compgeo.2023.105833.
[11] A. Zhang, L. Cheng, B. Cao, J. Yang, Temperature tracing test and numerical simulation study during leakage of earth-rock dam, Int. J. Therm. Sci. 192 (2023) 108449, https://doi.org/10.1016/j.ijthermalsci.2023.108449.
[12] H. Li, M. Yang, Application study of distributed optical Fiber seepage monitoring technology on embankment engineering, Appl. Sci. 14 (13) (2024), https://doi.org/10.3390/app14135362.
[13] S. Nan, J. Ren, F. Ni, L. Zhang, X. He, Heat tracing of embankment dam leakage: laboratory experiments and 2D numerical modelling, J. Hydrol. (Amst.) 608 (2022) 127663, https://doi.org/10.1016/j.jhydrol.2022.127663.
[14] B. Bekele, C. Song, J. Eun, S. Kim, Exploratory seepage detection in a laboratory-scale earthen dam based on distributed temperature sensing method, Geotech. Geol. Eng. 41 (2) (2023) 927–942, https://doi.org/10.1007/s10706-022-02315-2.
[15] B. Bekele, C. Song, B. Abualshar, A. Hunde, Real-time seepage health monitoring using spatial autocorrelation of distributed temperature data from fiber optic sensor, J. Civ. Struct. Heal. Monit. (2024), https://doi.org/10.1007/s13349-024-00868-9.
[16] H. Zhang Tao, Su, Experimental on distributed heating Fiber optic sensing for typical seepage of embankment, in: C.L.Y. Wang, Weiqiang Wang (Eds.), Hydraulic Structure and Hydrodynamics, Springer Nature Singapore, Singapore, 2025, pp. 269–281, https://doi.org/10.1007/978-981-97-7251-3_23.
[17] W. Kang, Understanding seepage in levees and exploring the applicability of using an optical-Fiber distributed temperature system and smoothing technique as a monitoring method, Sensors 23 (10) (2023), https://doi.org/10.3390/s23104780.
[18] W. Kang, S. Kim, E. Jang, Effect of seepage on sand levee failure due to lateral overtopping, Water (Basel) 16 (24) (2024), https://doi.org/10.3390/w16243617.
[19] Y. Ghafoori, Optimization of Early Seepage Detection in Embankments Using a Distributed Temperature System Based on fiber Optic Sensing, Ph.D. Thesis, University of Ljubljana, Ljubljana, 2023.
[20] A. D'Aniello, Detecting background leakages in water infrastructure with Fiber optic distributed temperature sensing: insights from a heat transfer-unsaturated flow model, Water Resour. Manag. 37 (2023), https://doi.org/10.1007/s11269-023-03617-7.
[21] X. Lu, et al., Influences of thermal dispersion on soil water flux estimates using heat pulse technique in saturated soils, Catena (Amst.) 167 (2018) 228–235, https://doi.org/10.1016/j.catena.2018.04.041.
[22] J.W. Hopmans, J. Šimunek, K.L. Bristow, Indirect estimation of soil thermal properties and water flux using heat pulse probe measurements: geometry and dispersion effects, Water Resour. Res. 38 (1) (2002), https://doi.org/10.1029/2000WR000071, pp. 7-1-7–14.
[23] A. Peters, T.L. Hohenbrink, S.C. Iden, M.Th. van Genuchten, W. Durner, Prediction of the absolute hydraulic conductivity function from soil water retention data, Hydrol. Earth Syst. Sci. 27 (7) (2023) 1565–1582, https://doi.org/10.5194/hess-27-1565-2023.
[24] A. Moradi, K.M. Smits, N. Lu, J.S. McCartney, Heat transfer in unsaturated soil with application to borehole thermal energy storage, Vadose Zone J. 15 (10) (Oct. 2016), https://doi.org/10.2136/vzj2016.03.0027 vzj2016.03.0027.
[25] H.-J.G. Diersch, FEFLOW: Finite Element Modeling of Flow, Mass and Heat Transport in Porous and Fractured Media, Springer, 2014, https://doi.org/10.1007/978-3-642-38739-5.
[26] M. Kaviany, Principles of Heat Transfer in Porous Media, Springer-Verlag, New York, USA, 1991, https://doi.org/10.1007/978-1-4684-0412-8.

[27] J. Bear, A. Verruijt, Modeling Groundwater Flow and Pollution, D. Reidel Publishing Company, Dordrecht, Holland, 1987, https://doi.org/10.1007/978-94-009-3379-8.
[28] A. Nield Donald, A. Bejan, Convection in Porous Media, Springer, New York, USA, 2006.
[29] U. Schindler, L. Müller, Soil hydraulic functions of international soils measured with the extended evaporation method (EEM) and the HYPROP device, Open Data J. Agric. Res. 3 (2017) (2017) 10–16, https://doi.org/10.4228/ZALF.2003.273.
[30] M.Th. van Genuchten, A closed-form equation for predicting the hydraulic conductivity of unsaturated soils, Soil Sci. Soc. Am. J. 44 (5) (1980) 892–898, https://doi.org/10.2136/sssaj1980.03615995004400050002x.
[31] Silixa Ltd, SILIXA XT-DTS Software Manual, Silixa Ltd, Elstree, UK, 2014.
[32] M.B. Hausner, F. Suárez, K.E. Glander, N. van de Giesen, J.S. Salker, S.W. Tyler, Calibrating single-ended Fiber-optic Raman spectra distributed temperature sensing data, Sensors 11 (11) (2011) 10859–10879, https://doi.org/10.3390/s111110859.
[33] ONSET, HOBO Data Loggers: Product Catalog [Online]. Available, https://www.onsetcomp.com/learning/catalogs, 2019.
[34] B.S. Hemingway, Quartz; heat capacities from 340 to 1000 K and revised values for the thermodynamic properties, Am. Mineral. 72 (3–4) (1987) 273–279.
[35] N. Zhang, X. Yu, A. Pradhan, A.J. Puppala, Thermal conductivity of Quartz Sands by Thermo-time domain reflectometry probe and model prediction, J. Mater. Civ. Eng. 27 (12) (2015), https://doi.org/10.1061/(asce)mt.1943-5533.0001332.
[36] H. Kiyohashi, S. Sasaki, H. Masuda, Effective thermal conductivity of silica sand as a filling material for crevices around radioactive-waste canisters, High Temp. High Press 35 (36) (2003) 179–192, https://doi.org/10.1068/htjr089.